European Congress on Computational Methods in Applied Sciences and Engineering
ECCOMAS 2000
Barcelona, 11-14 September 2000

DSMC SIMULATION OF SEPARATED FLOWS ABOUT FLARED BODIES AT HYPERSONIC CONDITIONS

James N. Moss*

*Aerothermodynamics Branch, NASA Langley Research Center, Hampton, VA 23681-2199, USA, email: j.n.moss@larc.nasa.gov, web page: http://abweb.larc.nasa.gov:8080//

Key words: hypersonic, low density, DSMC computations, shock/shock interactions, shock/boundary layer interactions, comparisons with measurements

Abstract. *This paper describes the results of a numerical study of interacting hypersonic flows at conditions produced in ground-based test facilities. The computations are made with the direct simulation Monte Carlo (DSMC) method of Bird. The focus is on Mach 10 flows about flared axisymmetric configurations, both hollow cylinder flares and double cones. The flow conditions are those for which experiments have or will be performed in the ONERA R5Ch low-density wind tunnel and the Calspan-University of Buffalo Research Center (CUBRC) Large Energy National Shock (LENS) tunnel. The range of flow conditions, model configurations, and model sizes provides a significant range of shock/shock and shock/boundary layer interactions at low Reynolds number conditions. Results presented will highlight the sensitivity of the calculations to grid resolution, contrast the differences in flow structure for hypersonic cold flows and those of more energetic but still low enthalpy flows, and compare the present results with experimental measurements for surface heating, pressure, and extent of separation.*

1 INTRODUCTION

Hypersonic separated flows produce shock/shock and shock/boundary layer interactions that create augmented aerothermal loads and reduced surface control effectiveness, issues critical to hypersonic vehicle design. To enhance the understanding of such flows, experimental and computational studies have been actively promoted by the NATO Research Technology Organization (RTO, formerly AGARD) for basic axisymmetric configurations and for a range of Reynolds numbers. The current study focuses on the low Reynolds number experimental conditions where separation and reattachment occur under laminar conditions and where the flow is assumed to be steady. Calculations are made by using the direct simulation Monte Carlo (DSMC) method of Bird [1] for both hollow cylinder-flare and double-cone models. The flow conditions simulated are those for which experiments have been or will be conducted in two facilities: the ONERA R5Ch Mach 10 low-density wind tunnel and the Calspan-University of Buffalo Research Center (CUBRC) Large Energy National Shock (LENS) tunnel.

The hollow cylinder-flare model has a sharp leading edge, a cylinder 101.7 mm long, and a 30° flare. The author has presented extensive calculations (refs. [2] - [7]) for the cylinder-flare model at the ONERA test conditions highlighting the noncontinuum and continuum aspects for the flow, the sensitivity to numerical simulation parameters, the agreement with measurements made in the ONERA wind tunnel, differences in two-dimensional (2D) and axisymmetric results, and comparisons with boundary layer (only cylinder or plate results) and Navier-Stokes solutions. These results are reviewed along with the presentation of new results that demonstrate the sensitivity of the calculations for the cylinder portion of the model to numerical parameters. Also, results of new calculations are included for more energetic flows, as produced in the LENS tunnel for a nominal test condition (Mach 9.6 nitrogen). For the LENS test conditions, calculations are presented for two models—the ONERA model configuration and a model with a much longer flare.

Calculations for the double-cone models [8] are for the same flow conditions as the hollow cylinder-flare study. For the double-cone configurations investigated, the shock/shock interactions are stronger than those for the hollow cylinder-flare models. The first cone half angle is 25°, while the second cone half angle is either 55° or 65°. These double cone geometries produce strong shock interactions because the attached shock from the first cone interacts with the detached bow shock from the second cone. Also, the outer shocks are modified by the separation and reattachment shocks where the extent of flow separation is significant for the combinations of model size and flow conditions examined. Results are presented that demonstrate the sensitivity of the surface results to numerical parameters, Reynolds number, and flow conditions.

2 DSMC Code

The DSMC code used in the current study is the general 2D/axisymmetric code of Bird [1],[9]. The molecular collisions are simulated with the variable hard sphere (VHS) molecular model. Energy exchange between kinetic and internal modes is controlled by the Larsen-Borgnakke statistical model [10]. For the present study, the simulations are performed by using nonreacting gas models while considering energy exchange between translational, rotational, and vibrational modes. A constant rotational relaxation collision number of 5 was used for the calculations. The vibrational collision number was 50. The reference conditions for the VHS model were as follows: reference temperature = 300 K, temperature exponent of the viscosity coefficient = 0.75, and reference diameters for O_2 and N_2 were 3.96 x 10^{-10} m and 4.07 x 10^{-10} m, respectively. The model surface is assumed to have a specified constant temperature. Full thermal accommodation and diffuse reflection are assumed for the gas-surface interactions.

Common to the DSMC simulations presented is the treatment of the computational domain griding, which consisted of an arbitrary number of regions. Each region is subdivided into cells, and the cells in selected regions are subdivided into subcells to enhance the spatial resolution used to select collision partners. In general, the cell dimensions within a region were nonuniform in both directions, with geometric stretching exceeding an order of magnitude in some regions. Also, the macroscopic quantities are time-averaged results extracted from the individual cells. Since the computational regions were not run with necessarily the same time step, it was essential that steady state conditions be established before generating the final time-averaged results. Steady state was assumed to occur when the total molecules used in the simulation, average molecules in each region, and surface quantities (locations and size of the separation region, heating, etc.) became essentially constant when sampled sequentially over significant time intervals.

3 CALCULATIONS FOR HOLLOW CYLINDER FLARE

The ONERA hollow cylinder-flare test case considered was formulated initially as one of the test problems concerning shock wave/boundary layer interactions in an AGARD Working Group 18 activity [11] for the validation of Navier-Stokes solvers for cold high-speed flows where the interactions produce large separated regions under laminar conditions. The initial test case generated considerable interest for code validation, as is evident by the AGARD activity [11] and several independent workshops. Interest in this problem continues with the expansion of test cases to include additional flow conditions and model sizes [12],[13] in the current Research Technology Organization (RTO, formally AGARD), working group 10 activities.

A motivation for investigating these test cases with DSMC has been to identify the level of grid resolution and related computational parameters that one must use to achieve accurate results for problems with complex interactions (where the grid resolution is important in directions other than the one normal to the surface). Furthermore, DSMC

codes provide a simulation capability that is valid across the entire flow spectrum of free molecular through continuum, a desirable feature for the current problems. However, there are practical limitations when using the DSMC approach due to excessive computational requirements as one moves well into the continuum regime for multiple-dimensional problems.

The current study includes numerical simulations for two sets of flow conditions and two hollow cylinder-flare models. Table 1 lists the free-stream and surface conditions for the experiments that have been conducted in the ONERA R5Ch low-density wind tunnel. Also included is a set of nominal flow conditions for a test scheduled to be performed in the LENS tunnel.

Details of the model configuration used in the ONERA tests are presented in Fig. 1. The hollow cylinder has a sharp leading edge with a bevel angle of 15° and is aligned parallel to the oncoming flow. The compression flare is inclined 30° to the cylinder and is terminated by a hollow cylindrical section. Additional information concerning model construction, materials, and instrumentation is given in refs. [14] and [6].

For the CUBRC tests, two hollow cylinder-flare configurations will be used as described in [12] and [13]—one that mimics the ONERA model (current calculations use the dimensions shown in Fig. 1 for describing the model outer surface) and a model with a much longer flare. For the long-flare model, the horizontal length of the flare is 118.28 mm rather than the 43.3 mm shown in Fig. 1, and the model terminates at the end of the flare.

Table 1: Free-stream and surface conditions

Facility	V_∞, m/s	ρ_∞, kg/m^3	n_∞, m^{-3}	T_∞, K	p_∞, N/m^2	Gas	M_∞	T_W, K
ONERA R5Ch	1 418.7	4.303×10^{-4}	0.895×10^{22}	51.0	6.30	Air	9.91	293.0
CUBRC LENS	2 718.6	6.808×10^{-4}	1.463×10^{22}	194.1	39.21	N_2	9.56	297.8

3.1 Previous Results and Findings for the ONERA R5Ch Tests

Figures 2 through 8 present results of the calculations first reported in refs. [4] and [5] that describe the flow-field features and surface results for the ONERA hollow cylinder-flare test case. The experimental value for free-stream Reynolds number is 18 916, where the viscosity (3.29 x 10^{-6} Pa $*$ s) is given by the Sutherland expression and the characteristic dimension is the cylinder length L. Also presented are comparisons of the surface results for heating, pressure, and the extent of separation with the experimental measurements described in refs. [14] , [6], and [7]. The current results are those obtained with the finest grid resulting from the grid resolution study described in ref. [4]. The previous calculations show that the extent of separation is quite sensitive to the grid—a much smaller separation region is obtained with a coarse grid. Data included in Fig. 2 provide

information concerning the grid and simulation parameters. A four-region computational domain was used where each cell was subdivided into four subcells (2 x 2). The time step in each of the four regions had values of 75, 75, 28, and 15 ns, respectively.

General flow features for this test case are evident in Figs. 2 and 3. Figure 2 shows selected Mach contours and streamlines while Fig. 3 presents the normalized density contours. Evident is a large separation region characterized by a single vortex embedded in the subsonic flow region. Calculated locations for separation and reattachment (denoted by S and R, respectively) are 76.76 mm and 134.4 mm downstream of the cylinder leading edge. The shock/shock interaction occurs near the end of the flare where the shock layer thickness is at a minimum and the density is at a maximum, equal to 14.4 times the free-stream value.

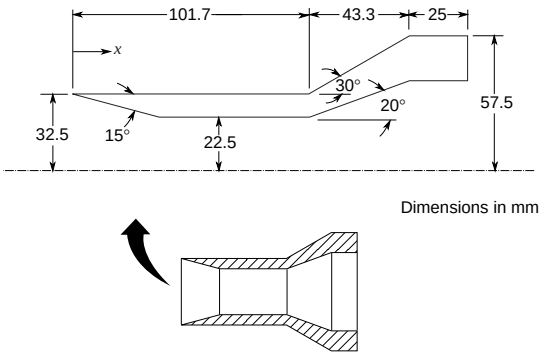

Figure 1: Hollow cylinder-flare model (x measured from leading edge and L = 101.7 mm).

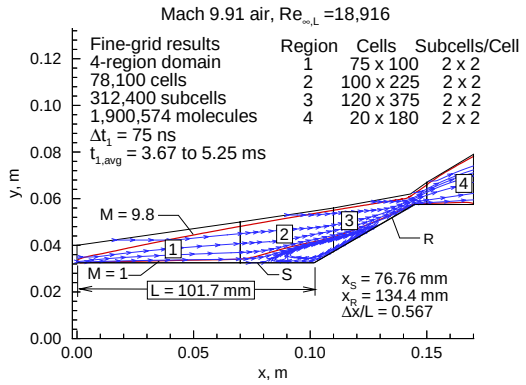

Figure 2: Flow structure and simulation parameters for ONERA hollow cylinder flare.

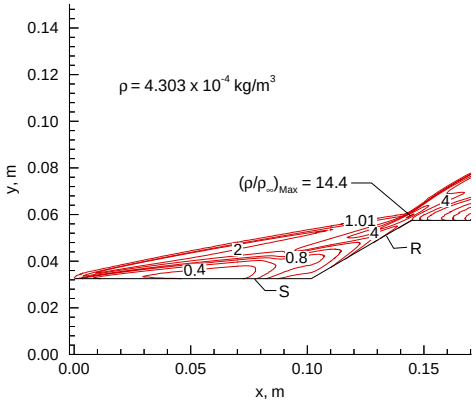

Figure 3: Density contours for ONERA hollow cylinder flare.

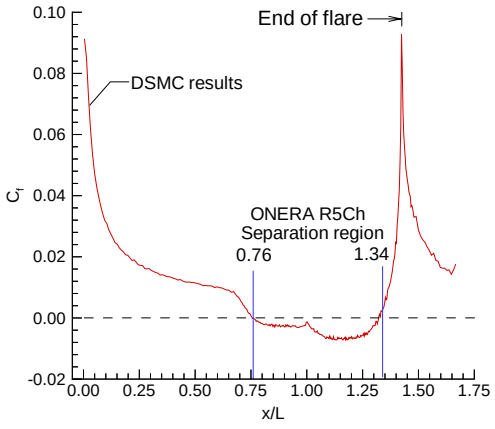

Figure 4: Skin friction coefficient and extent of separation (oil-flow data from experiments).

Figures 4 through 6 present the calculated surface results for skin friction coefficient, heating rate, and pressure coefficient as a function of the distance from the cylinder

leading edge (normalized by the cylinder length L). Maximum values for friction, heating rate, and pressure occur on the flare at a location downstream of reattachment—very close to the end of the flare located at x/L = 1.426. Included in these figures are the results of the experimental measurements [6], [7] for the extent of separation as inferred from oil flow measurements, heating rates extracted by using a thin-film technique, and surface pressure inferred from variable reluctance differential transducers connected to model pressure taps by tubes.

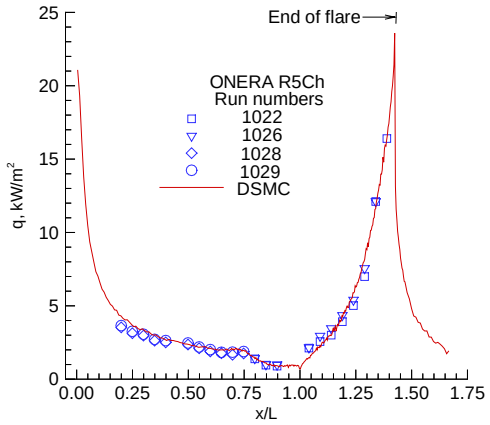

Figure 5: Heat-transfer rate distributions.

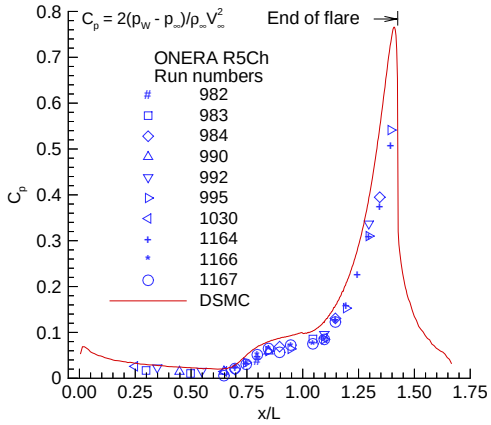

Figure 6: Pressure coefficient distributions.

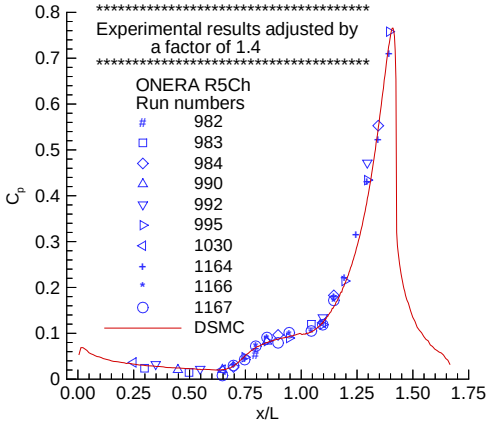

Figure 7: Pressure coefficients—experimental data adjusted.

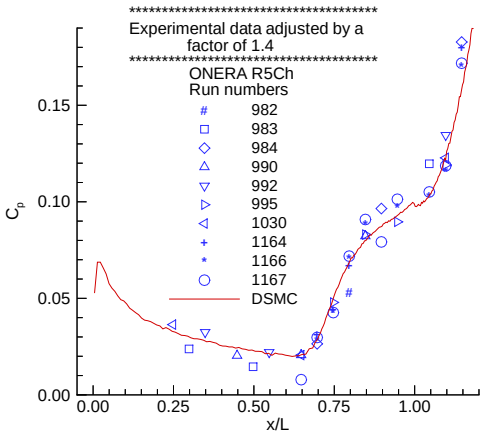

Figure 8: Cylinder pressure coefficients—experimental data adjusted.

Agreement between the calculated and the measured results are very good for the extent of separation and the heating rate distribution; however, there are noticeable differences for the pressure distribution. The separation location is the same for both sets of results. The calculated reattachment location occurs, however, somewhat forward of

the experimental value, and the extent of the calculated separation ($\Delta x/L$) is 98% of the measurement. The heating-rate distributions are characteristic of those for laminar flows in that the heating shows an initial decrease at the location of separation ($\Delta x/L = 0.76$), a cusp-like behavior at the juncture, and a rapid increase along the flare.

Among the surface quantities, the agreement between the current calculations and measurements is the poorest for pressure. This discrepancy is particularly puzzling since the agreement for both heat transfer and the locations for separation and reattachment are very good. The trends of the two data sets are qualitatively consistent; however, the computational results are consistently higher than the measured values. As first pointed out in Ref. [4], the 42% discrepancy near the peak pressure location on the flare is very obvious; however, differences of this magnitude are also present along the hollow cylinder. In fact, this difference is a constant. If the experimental pressure values are multiplied by a factor of 1.4, agreement between the two data sets becomes very good, as shown in Figs. 7 and 8, where Fig. 8 presents an enlarged view focusing primarily on the cylinder. Additional results are presented in section 3.2 that address the lack of agreement along the cylinder between calculation and measurement.

Flow-field density measurements have also been performed at ONERA for the hollow cylinder-flare model by detecting X-ray emissions from the gas produced by electron beam impact. The experimental results have been compared [7] with numerical results obtained by using the current DSMC results and two Navier Stokes codes. The agreement between measurements and calculations is somewhat mixed since neither DSMC nor Navier Stokes results provided consistent agreement with the measurements made at three locations ($x/L = 0.3$, 0.6 and 0.76) along the cylinder. Details concerning these measurements and comparisons are given in Ref. [7].

3.2 Effect of Computational Parameters on Hollow Cylinder Results

This section presents the results of calculations for only the hollow cylinder portion of the ONERA model to address the discrepancy observed between measured and calculated surface pressures. With confidence in the ability to computationally resolve and accurately predict the flow conditions along the cylinder, additional calculations were made that focus on the sensitivity of the calculated results to numerical parameters. The focus is on the cylinder terminated at $x = 70$ mm, the interface location between regions 1 and 2 (Fig. 2). The purpose of this portion of the study is to examine the sensitivity of the surface and flow-field results to variations in the numerical parameters used in the results discussed earlier; in particular, to determine if the calculated surface pressure is influenced by additional refinements and leading edge treatments (amount of flow domain included in the computational domain and grid resolution). The particular parameters for which variations were made are the magnitude of the time step, grid resolution, and the treatment given to the model leading edge. As shown in Figs. 9 though 12, the results for these cases are compared to each other and to the hollow cylinder-flare results previously presented.

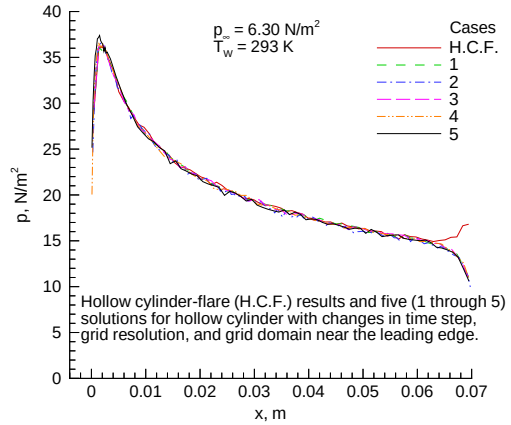

Figure 9: Effect of simulation parameters on cylinder pressure distributions.

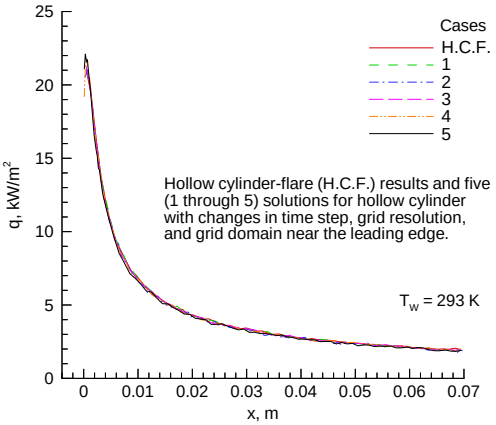

Figure 10: Effect of simulation parameters on cylinder heating-rate distributions.

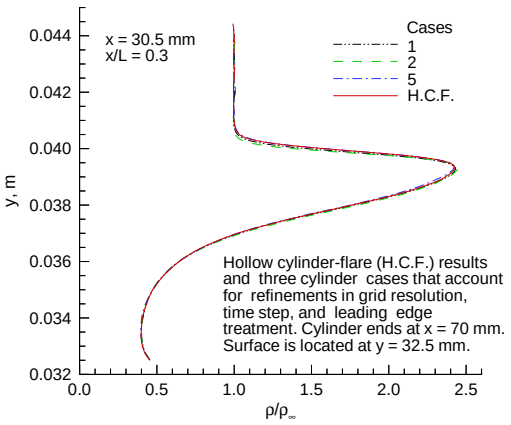

Figure 11: Effect of simulation parameters on calculated density profiles (x/L = 0.3).

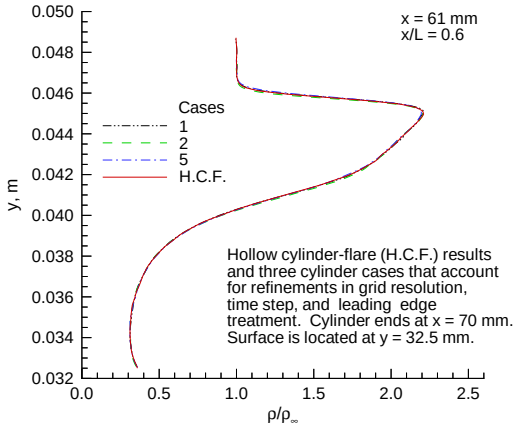

Figure 12: Effect of simulation parameters on calculated density profiles (x/L = 0.6).

Surface results for pressure and heating rate are given in Figs. 9 and 10, respectively. The influence of the flare on the hollow cylinder-flare (denoted as H.C.F in Figs. 9-11) results extends slightly upstream of the x = 70 mm location, clearly evident in the surface pressure distribution (Fig. 9) but not evident in the heating-rate distribution (Fig. 10). Also, the outflow boundary condition imposed (free stream at the end of the cylinder) has an influence on the surface pressure results that extends about 6 mm upstream of the cylinder termination. The parametric variations for each of the five cylinder calculations are as follows: Case 1 was a one-region computational domain identical to that used in the H.S.F. simulation (see Fig. 2); for Case 2, the number of cells and subcells were increased by a factor of three (140 x 150 cells), and the time step was 20% of that for Case 1 (15 ns); Case 3 used a time step of 25 ns and the same cell resolution as H.C.F. and Case 1; Case 4

used a time step of 25 ns and the same grid resolution as the H.C.F. but had two extra regions, with additional treatment in front of and downstream of the leading edge (a region upstream of the leading edge [-3 mm] and a region that extended a short distance [3 mm] downstream of the leading edge with five times the Δx resolution of the H.S.F case). Case 5 differed from Case 4 in that it included two additional regions to account for the influence of the beveled leading edge underside. Common to all the solutions were the four subcells/cell and a scaling of real to simulated molecules such that there were, on average, approximately 25 simulated molecules per cell. When the surface results for pressure and heating rate distributions are compared with the H.S.F. results, there is no effect other than the expected results very near the leading edge—as the cell dimension in the x-direction (Δx) decreases near the leading edge, one gets an improved definition of the surface quantities where a local maximum occurs and then decreases in value as the leading edge is approached (quantities are decreasing toward their free molecular values but will not achieve the free molecular values because of upstream influence). As for the impact of these additional refinements on the downstream flow-field quantities, no impact is evident on the density profiles at x/L locations of 0.3 and 0.6, as shown in Figs. 11 and 12, respectively.

Based on the findings of this section, it is believed that the DSMC results presented earlier for surface pressure are correct for the cylinder and should be reasonably accurate for the flare, based on a constant discrepancy of 40% with measurements for both cylinder and flare. Also, the current DSMC results are in good agreement with those obtained by Markelov et al. [16] for the ONERA test case, in which a different DSMC code was used.

3.3 Computational Results for LENS Flow Conditions

This section presents results of DSMC calculations for flow about two hollow cylinder-flare models at a nominal LENS flow condition (Table 1), where the flow is Mach 9.57 nitrogen at a free-stream Reynolds number of 14 920 (characteristic length is the cylinder length, L = 101.7 mm, and the viscosity is given by the VHS [1] model). The flow is more energetic than the R5Ch conditions; however, the flow enthalpy is still quite low and chemical reactions are neglected for this test case condition. As previously discussed, the short flare model was assumed to have the same outer surface dimensions as the ONERA model (Fig. 1) while the long-flare model has simply an extended flare with the model terminated at the end of the flare. The long-flare model was included [12] in the experimental program to allow for a complete pressure recovery on the flare, thus making a more straightforward comparison with theoretical models. The current results provide an indication of the sensitivity of the DSMC calculations to grid resolution, show that the extent of separation is much smaller than that for the R5Ch flow conditions, show that the results for the long and short flare are essentially identical within the domains common to the two models, and provide information concerning the general features of the surface results and flow-field structure.

Figures 13 and 14 provide information describing the computational domain, simula-

tion parameters, flow structure (selected Mach contours and streamlines), and calculated locations for separation and reattachment for the short and long flare CUBRC models, respectively. (The symbol F in Figs. 13 and 14 denotes the ratio of real to simulated molecules.) These results are for the finest grid calculations resulting from several computations where grid refinement and sensitivity studies were performed. Figure 15 is an example of the results for the long flare model showing the sensitivity of heating rate to different combinations of regions, cells, and subcells—a factor of 27 in subcell resolution. The effect of grid resolution on heating shows the expected trend of decreased heating with improved grid resolution outside the surface areas influenced by flow separation. Also, the size of the separation zone increases with improved grid resolution, as indicated by the tabulated results for $\Delta x/L$ included in Fig. 15. The peak heating downstream of reattachment is slightly higher for the finer grid results.

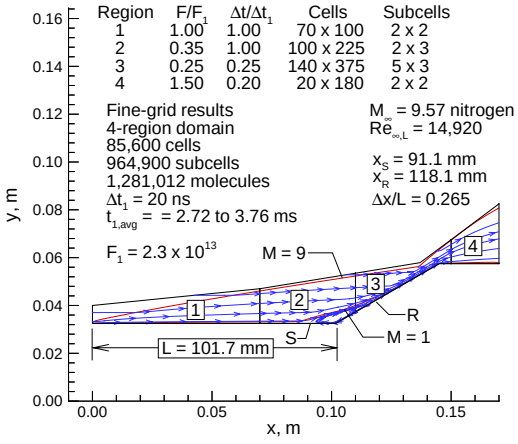

Figure 13: Flow structure and solution parameters for CUBRC model with short flare.

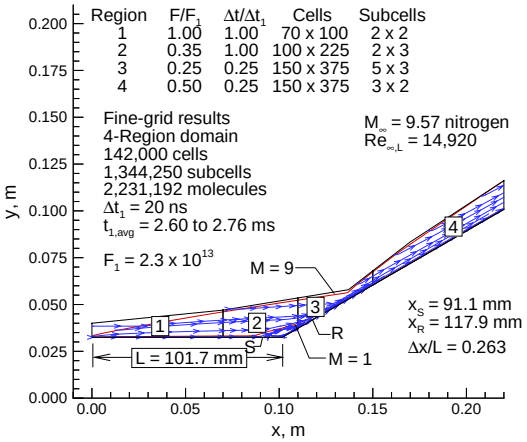

Figure 14: Flow structure and solution parameters for CUBRC model with long flare.

The results presented in Fig. 15 do not demonstrate grid convergence; however, results for the short flare model, where the grid was identical to that for the long flare model for regions 1 through 3, showed that the surface results were in close agreement for two solutions, where one solution had the cell/subcell arrangement given in Fig.13 (same as for the long flare solution for regions 1 through 3) and one with the same number of cells (85 600) but only about half the number of subcells (531 200).

Comparisons of surface results for the short and long flare models are presented for heating coefficient, pressure coefficient, and skin friction coefficient in Figs 16, 17, and 18, respectively. The results show that the surface quantities are essentially identical for surfaces common to the short and long flare models. For this particular LENS nominal test condition, the extent of separation is only 47% of that calculated and measured for the ONERA R5Ch test condition. With the smaller extent of separation, the calculations

suggest that the short flare is sufficiently long to negate any influence of the expansion at the end of the flare on the location of reattachment. However, the end of flare expansion produces a thinning of the boundary layer and significant changes in the surface quantities—decreasing pressure (Fig. 17) and increasing heating (Fig. 16) and friction (Fig. 18). The same trends are evident for the short-flare model where the flow expands on to the cylindrical extension at x = 0.145, as is clearly evident in the heating and friction results (also examine Fig. 19).

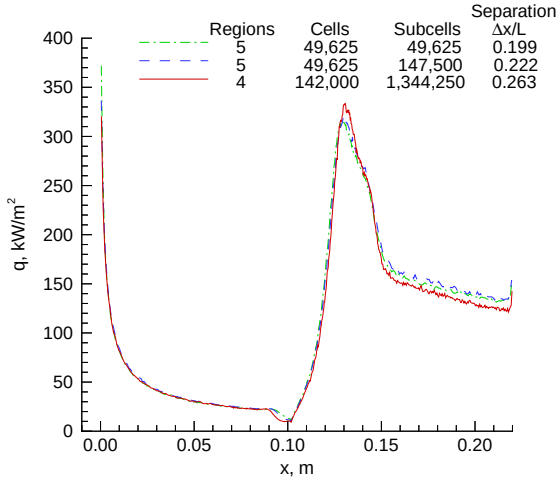

Figure 15: Effect of grid on heating rate—long flare at a LENS flow condition.

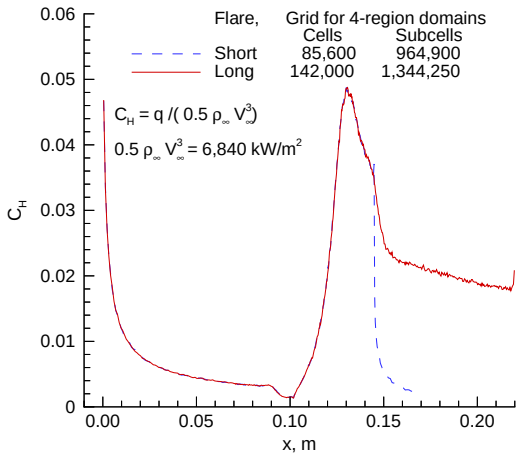

Figure 16: Heat-transfer coefficient results for a nominal LENS test condition.

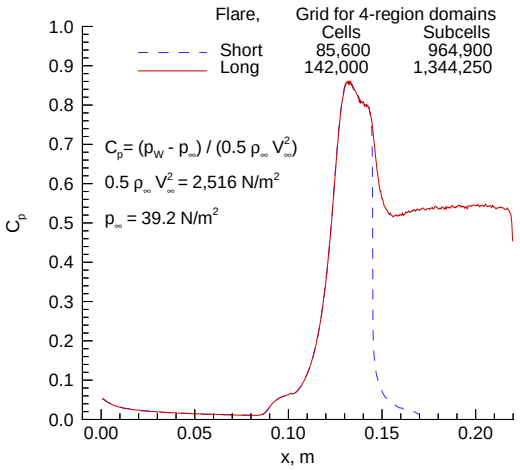

Figure 17: Pressure coefficient results for a nominal LENS flow condition.

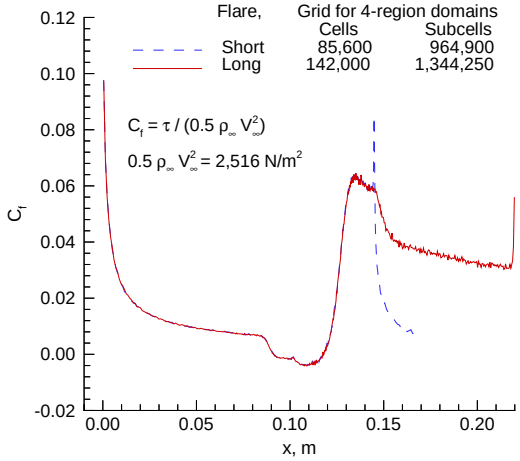

Figure 18: Skin friction coefficient results for a nominal LENS flow condition.

Composite plots for heating rate, pressure, and skin friction are given in Figs. 19 and 20 for the short and long flare models, respectively. These data sets provide information

on the correlation of the three surface quantities and explain how they are influenced by separation. The general qualitative features are the same as previously discussed for the R5Ch test conditions.

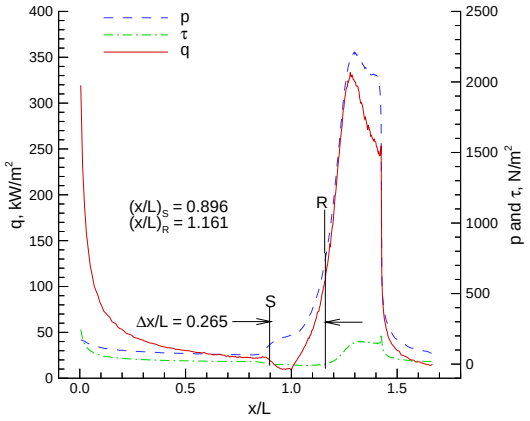

Figure 19: DSMC surface results for a nominal LENS condition (short flare).

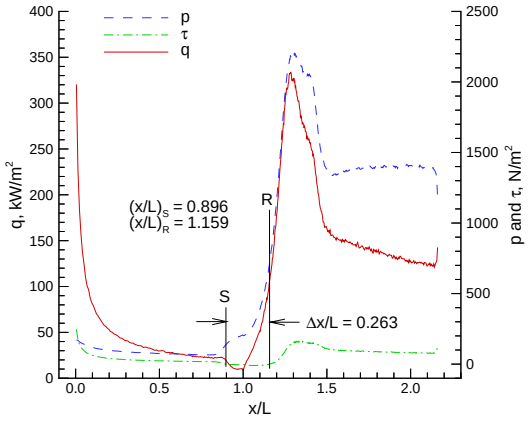

Figure 20: DSMC surface results for a nominal LENS condition (long flare).

Figures 21 through 24 provide information describing the flow structure for the short flare. Contours for nondimensional density, overall kinetic temperature, and scalar pressure (nkT, where T is the overall kinetic temperature) are included. The flare-induced adverse pressure gradient is evident in Fig. 23 where the isopressure lines coalesce into a separation shock that compresses the flow to a maximum density of 29.6 times the free-stream value. An enlarged view of the scalar pressure contours in the reattachment region and beyond are presented in Fig. 24. Along the surface and downstream of reattachment are the locations for maximum density and scalar pressure, with magnitudes equal to 29.6 and 57.2 times their respective free-stream values. When the current calculated results for the LENS condition are compared with the calculated results for the R5Ch flow conditions (see ref. [4]), the maximum density is 3.25 times greater and occurs at the surface rather than in the shock layer as it does for the R5Ch case (Fig. 3). Also, the temperatures are much higher, the maximum temperature being 2.8 times greater. For the maximum scalar pressure, the calculated LENS value is 6.2 times that calculated for the R5Ch condition.

Figures 25 through 28 present calculated surface normal profiles for the CUBRC model with a short flare. Included are six body station profiles along the cylinder where the surface is located at y = 32.5 mm. Data for four variables—density, scalar pressure, overall kinetic temperature, and tangential velocity—are presented. These profiles help to identify some of the thermal nonequilibrium aspects of the flow with evidence of temperature and velocity jump at the surface, where the magnitude of the jump increases as the leading edge is approached. Also note that for the nonequilibrium situations, the scalar pressure will be different from the normal force per unit area on an element of solid surface; that is,

the surface normal force and the gas scalar pressure adjacent to the surface element will be different, as they are for the present case, particularly near the model leading edge.

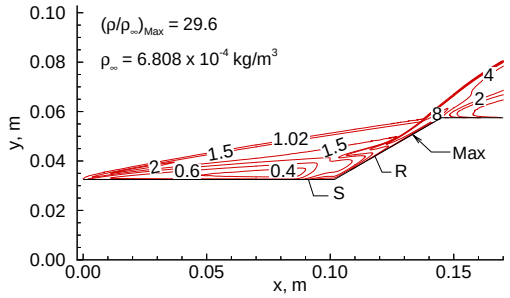

Figure 21: Density contours for a nominal LENS condition (short flare).

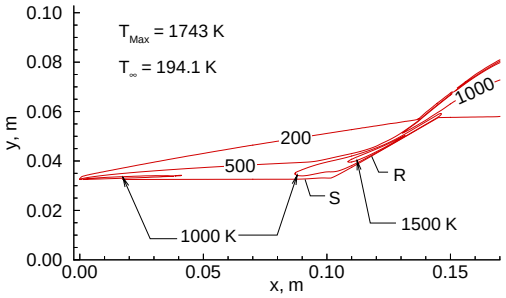

Figure 22: Overall kinetic temperature contours for a LENS condition (short flare).

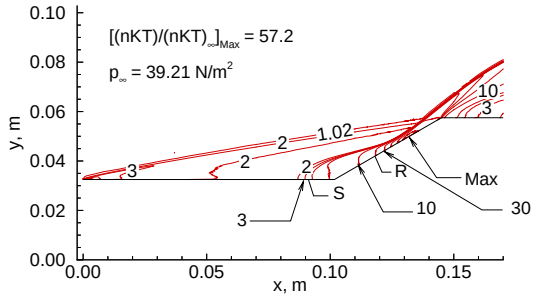

Figure 23: Scalar pressure contours for a nominal LENS condition (short flare).

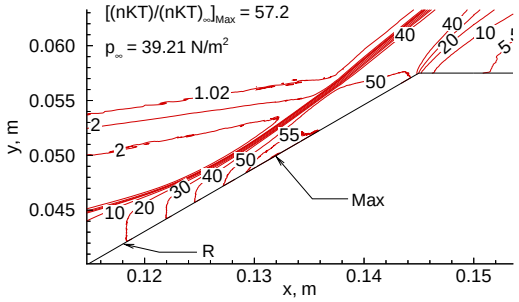

Figure 24: Scalar pressure contours along flare for a nominal LENS condition (short flare).

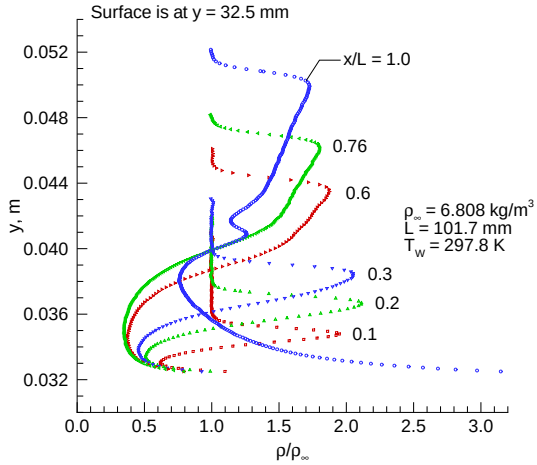

Figure 25: Density profiles for a nominal LENS condition (short flare).

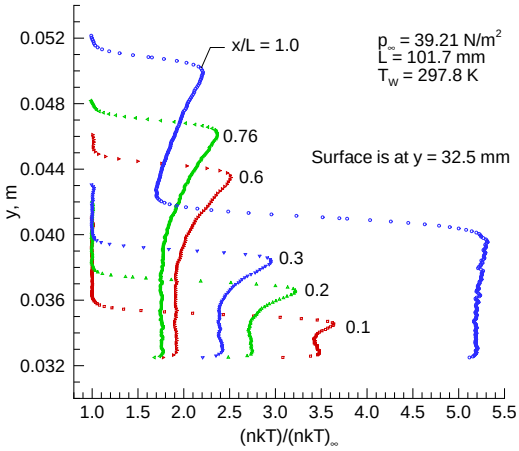

Figure 26: Scalar pressure profiles for a nominal LENS condition (short flare).

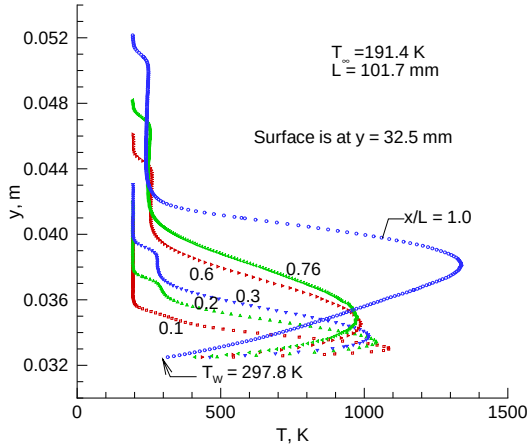

Figure 27: Overall kinetic temperature profiles for a nominal LENS condition (short flare).

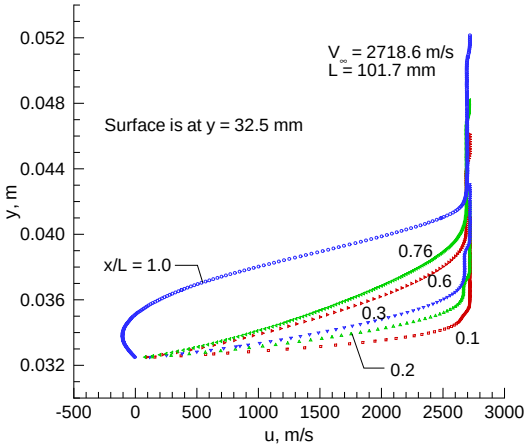

Figure 28: Tangential velocity profiles for a nominal LENS condition (short flare).

For the x/L = 0.1 station, the temperature and tangential velocity profiles exhibit the characteristics of a merged layer. Farther downstream, the profiles exhibit a distinct inviscid layer behind the leading edge shock. From the density profiles, it is evident that the leading edge shock strength has reached an initial maximum near the x/L station of 0.2 and continues to decrease in strength until the shock/shock interaction region is encountered.

The compression wavelets originating upstream of separation (Fig. 23) coalesce into a shock before the outer edge of the boundary layer is reached, with the deflection of the inviscid flow lagging behind that near the surface. Thus, the compression of the flow in the boundary layer [15] varies from a somewhat gradual process, adjacent to the surface, to an oblique shock jump near the outer edge. The pressure profile at the x/L = 1.0 station (Fig. 26) illustrates this behavior where the pressure behind the leading edge shock is approximately two times the free-stream value but increases to approximately five times free stream behind the oblique separation shock.

4 CALCULATIONS FOR DOUBLE CONES

The results presented in this section are from ref. [8] where DSMC calculations were made for both the ONERA R5Ch and the CUBRC LENS flow conditions for model configurations that have been or will be tested. These results are included to highlight results where the shock/shock interactions are much stronger than those previously discussed for the hollow cylinder-flare cases. For the double-cone models investigated, the first cone half angle is 25°, while the second cone half angle is either 55° or 65°.

4.1 25°/65° Cones at Mach 9.9 Air Flow—ONERA R5Ch Conditions

Calculations presented in this section are an extension of those reported in refs. [4] and [5], where the flow about a sharp double-cone model (25°/65°) with a maximum diameter of 132.893 mm was calculated with both DSMC and Navier Stokes codes for Reynolds numbers ranging from 24 719 to 247. This Reynolds number range was achieved by using the R5Ch nominal free-stream flow conditions (highest Reynolds number) and then parametrically reducing the free-stream density. The current results are those for smaller scale models with diameters between 66.4 and 121.0 mm. The maximum diameter of the current model configuration that can be tested in the R5Ch wind tunnel is near 70 mm, or about half the model size used in the previous studies. The configuration is such that the lengths of the first and second cones are equal ($L_1 = L_2$, Fig. 29).

Figures 29 through 31 present representative results of the calculations. The nature of the shock interactions is demonstrated in Fig. 29 by using the fine grid results for the 66.4-mm-diameter model, a model size that the ONERA R5Ch wind tunnel should be able to accommodate. Selected Mach contours are shown in which a large subsonic region is located in front of the second cone. Locations for flow separation and reattachment along the surface are denoted by S and R, respectively. Also evident is the influence of the separation shock on the oblique shock that is produced by the first cone, resulting in a triple point (T. P.) followed by a stronger transmitted shock that interacts with the stronger bow shock of the second cone—creating a second triple point. These shock/shock and shock/boundary layer interactions are induced by the larger cone and produce a significant separation region characterized by a single vortex, indicated by streamlines embedded within the subsonic region near the intersecting cones. The general flow structure evident for the 66.45-mm-diameter model is that found for the larger 25°/65° models. However, when the model diameter is increased to 132.9 mm (results from ref. [5]), secondary vortices were evident, and a Navier-Stokes computation indicated some unsteadiness (small oscillations of separation location). Undoubtedly, the flow would become unsteady for larger models, as is demonstrated by the rapid growth of the extent of separation presented in Fig. 31.

Also included in Fig. 29 is information concerning the computational domain, which consisted of eight arbitrary regions. Each region is subdivided into cells, and the cells in selected regions are subdivided into subcells to enhance the spatial resolution used to select collision partners. Time step information for region one and the time interval for which the time-averaged results were obtained are included in Fig. 29.

Figure 30 presents the corresponding surface results—heating rate, pressure, and skin friction—for the 66.45-mm-diameter model. The variable s denotes the model wetted length measured from the cone vertex. Results are for a fine-grid solution, a solution for which the surface results and extent of separation indicate grid independence [8]. The qualitative features of the surface data are consistent with experimental measurements [15] for laminar separated flows. First, the separation position is in close agreement with

the location of the first inflection point (maximum slope) of the initial pressure rise and the location where the heat transfer rate decreases significantly with respect to the single cone results. Second, the pressure reaches a plateau for a significantly large separation region, while the heat transfer is significantly reduced. Third, at or preceding the intersection of the two cones, the heat transfer experiences a minimum and then increases rapidly, as does the pressure, with increasing distance along the second cone.

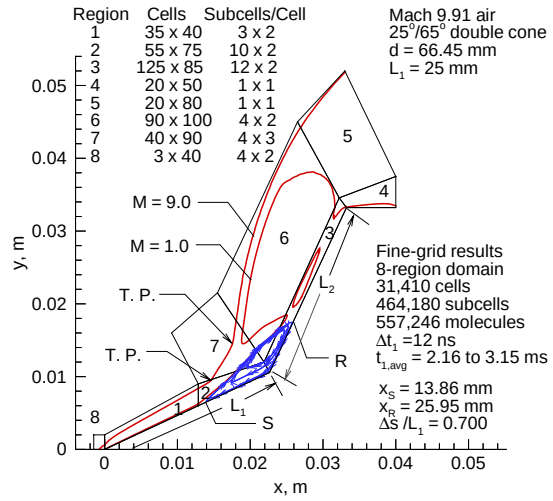

Figure 29: Flow structure and simulation parameters 25°/65° double cone (R5Ch flow).

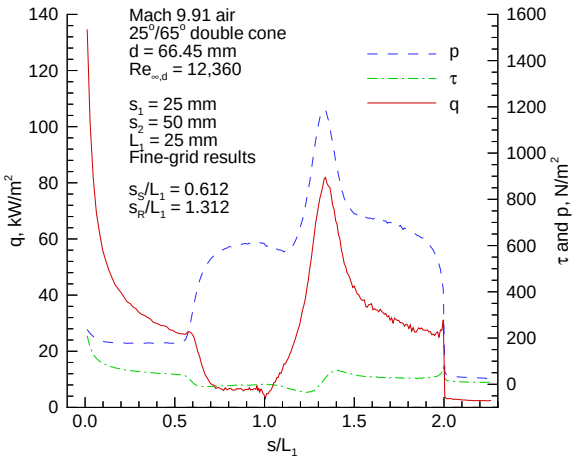

Figure 30: Calculated surface results for double-cone model at R5Ch flow conditions.

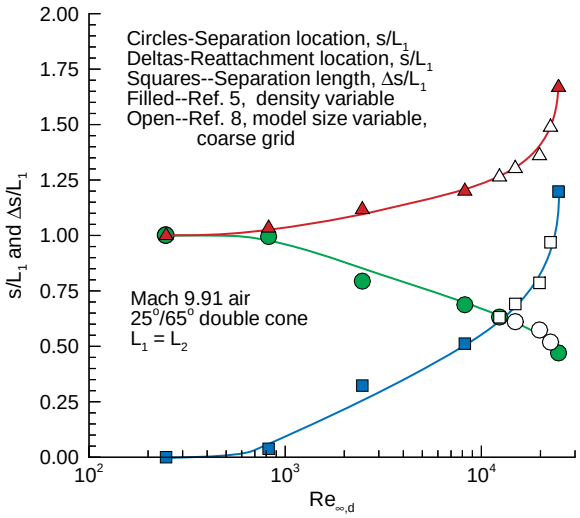

Figure 31: Separation data as a function of Reynolds number for R5Ch flow conditions.

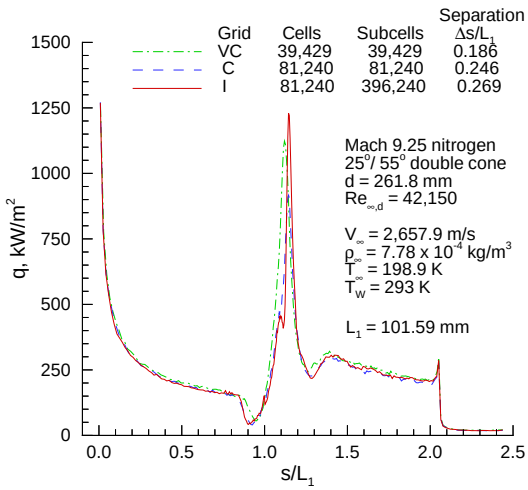

Figure 32: Effect of grid on heating-rate results for a pretest nominal LENS flow condition.

The sensitivity of the extent of separation to Reynolds number is presented in Fig. 31, where the results are a summary of those presented in ref. [5] (constant model diameter

of 132.9 mm and varying the free-stream density) and ref. [8] (the R5Ch flow conditions and varying the model diameter). The two data sets show a consistent trend: the extent of separation increasing with Reynolds number and a very rapid increase in separation near a Reynolds number of 25 000. For the conditions investigated, the calculations show that separation persists for Reynolds numbers as low as about 800.

4.2 25°/55° Cones at Mach 9.6 Nitrogen Flow—CUBRC LENS Conditions

This section focuses on results for the CUBRC LENS flow conditions where the maximum model diameter is 261.8 mm. The initial calculations were made for pretest nominal conditions (included in Fig. 32). A grid sensitivity study was conducted, and the results of this study, as it impacts the extent of separation ($\Delta s/L_1$) and surface heating-rate distributions, are presented in Fig. 32. The qualitative characterization of the grid listed in Fig. 32 is I for intermediate, C for coarse, and VC for very coarse. The finest grid used in this exercise is described as intermediate because grid independence was not demonstrated—additional grid refinement is necessary to indicate whether the current intermediate grid is adequate.

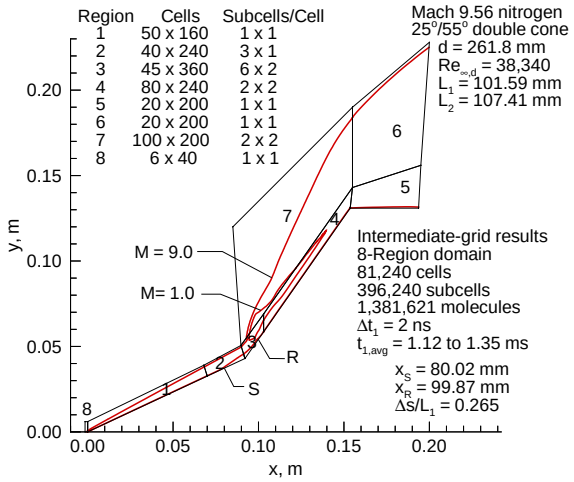

Figure 33: Flow structure and simulation parameters for 25°/55° double cone (LENS flow).

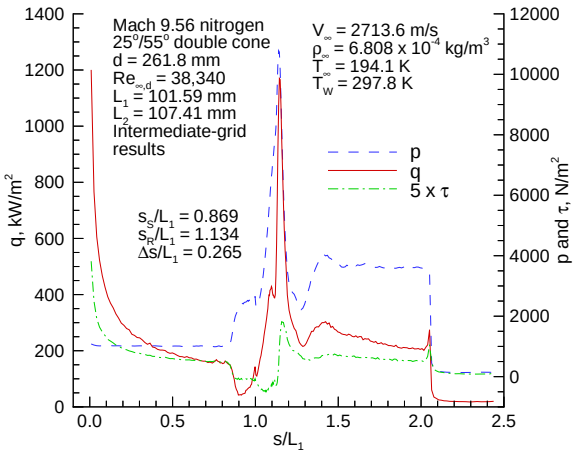

Figure 34: Calculated surface results for double-cone model at a LENS test condition.

Once information became available as to the actual test conditions used in the CUBRC experiments, the finest grid used in the pretest grid investigation was then used to make a calculation for the actual LENS test conditions (free-stream conditions included in Fig. 34), and selected results are presented in Figs. 33 and 34. The general features of the shock layer structure are given in Fig. 33 where selected Mach contours are included, along with details of the numerical parameters used in the simulation. Values for the surface quantities are shown in Fig. 34. For the surface pressure distribution, the calculated values outside the region influenced by the shock/boundary layer interactions are in close

agreement with the inviscid cone values (ref. [17]) of 948 N/m^2 along the 25° cone and 3710 N/m^2 along the 55° cone. Details concerning the flow structure are presented in ref. [8] where the calculations show that the maximum values for density and scalar pressure are 155 and 319 times their respective free-stream values and that there is a maximum overall kinetic temperature of 3104 K. Comparisons of translational and internal temperature profiles show that the nonequilibrium effects are confined primarily to the outer bow shock crossings. Opportunities will exist for comparing the present results with the experimental measurements (heating-rate and pressure distributions) that have been completed when the CUBRC data are released.

5 CONCLUDING REMARKS

Results of a computational study are presented for Mach 10 flow about hollow cylinder flare and sharp double cone models where the combination of model configurations, size, and flow conditions produce a significant range of shock/shock and shock/boundary layer interactions. The computations are made with the direct simulation Monte Carlo (DSMC) method, hence, low Reynolds number flows. The results presented provide insight into the nature of the shock interactions, their impact on surface quantities, and the sensitivity of the results to computational parameters for flow conditions that can be produced in current ground-based facilities.

Results of the hollow cylinder-flare calculations are compared with the experimental surface measurements made in the ONERA R5Ch wind tunnel (Mach 9.91 air at a $Re_{\infty,L}$ = 18 916). The extent of the calculated separation region is very sensitive to the grid resolution used—a coarse grid results in a smaller separation region. Results for the finest grid investigated show very good agreement with the experimental measurements for the separation and reattachment locations and surface heating. For surface pressure, the agreement between calculation and measurement is poor—the calculated values are uniformly high along both the cylinder and flare by a factor of 1.4. Additional DSMC calculations are made for the cylinder to examine the impact of additional refinement of solution parameters and leading edge treatment, and the results show no significant impact on the previously reported results. Based on these findings, it is believed the DSMC results for surface pressure are correct along the cylinder and should be reasonably accurate for the flare.

Also, DSMC results are presented for two hollow cylinder-flare models (one having the same outer surface as the ONERA model and one with a longer flare) that will be tested in the LENS facility at a proposed nominal test condition (Mach 9.57 nitrogen at a $Re_{\infty,L}$ = 14 920). Information concerning the effect of grid resolution is presented along with detailed data concerning surface results and flow structure. For the LENS test case, the extent of separation is much smaller than that calculated and measured for the ONERA tests, and the calculated surface results are essentially identical for the long and short flare models.

For the double cone models, the extent of separation as a function of free-stream

Reynolds number is demonstrated for hypersonic cold flow conditions, and the current results are shown to be consistent with previous calculations. These results are for the ONERA R5Ch wind tunnel flow conditions and 25°/65° double-cone models. Calculated results are presented for free-stream Reynolds numbers (based on maximum body diameter) of 247 to 24 719. Preliminary tests in the R5Ch tunnel have demonstrated that experiments can be conducted on this double-cone configuration for Reynolds numbers as large as 12 000. Computations were also made for a higher enthalpy test conducted in the CUBRC LENS impulse facility with a much larger diameter model and a 25°/55° double-cone configuration. Results of a grid sensitivity investigation are discussed, and surface results are presented for a test condition that has been conducted (Mach 9.56 nitrogen at a $Re_{\infty,L} = 38\,340$). Opportunities should exist for comparing the current results with experimental measurements for surface heating and pressure distributions.

6 ACKNOWLEDGMENTS

The author wishes to acknowledge the assistance of B. Chanetz and T. Pot of ONERA, Chalais-Meudon, for providing detailed information regarding their experiments and the results of their measurements. Also, the author wishes to acknowledge the assistance of Michael Holden of CUBRC for providing information regarding the model configurations and flow conditions used in the LENS tests.

REFERENCES

[1] Bird, G. A.; *Molecular Gas Dynamics and the Direct Simulation of Gas Flows*. Oxford: Clarendon Press, 1994.

[2] Moss, J. N., Dogra, V. K., and Price, J. M.; DSMC Simulations for a Hollow Cylinder-Flare Configuration. AIAA Paper 94-2015, June 1994.

[3] Moss, J. N., Dogra, V. K., Price, J. M., and Hash, D. B.; Comparison of DSMC and Experimental Results for Hypersonic External Flows. AIAA Paper 95-2028, June 1995.

[4] Moss, J. N., and Olejniczak, J.; Shock-Wave/Boundary-Layer Interactions in Hypersonic Low Density Flows. AIAA Paper 98-2668, 1998.

[5] Moss, J. N., Olejniczak, J., Chanetz, B., and Pot, T.; Hypersonic Separated Flows at Low Reynolds Number Conditions. *Proceedings of the* 21^{st} *International Symposium on Rarefied Gas Dynamics*, Brun, Campargue, Gatignol, and Lengrand, eds., Cepadues-Editions, Toulouse, France, Vol. II, 1999, pp. 617-624.

[6] Chanetz, B., Benay, R., Bousquet, J.-M., Bur, R., Pot, T., Grasso, F. and Moss, J.; Experimental and Numerical Study of the Laminar Separation in Hypersonic Flow. *Aerospace Science and Technology,* No. 3, 1998, pp. 205-218.

[7] Chanetz, B., Bur, R., Pot, T., Pigache, D., Grasso, F., and Moss, J.; Experimental and Numerical Study of the Laminar Separation in Hypersonic Flow. Paper presented at ECCOMAS 2000, Barcelona, Spain, Sept. 11-14, 2000.

[8] Moss, J. N.; *DSMC Simulations of Shock Interactions About Sharp Double Cones.* presented at the 22^{nd} International Symposium on Rarefied Gas Dynamics, Sydney, Australia, July 9-14, 2000. Available as NASA TM-2000-210318, August 2000.

[9] Bird, G. A.; The G2/A3 Program System Users Manual. Version 1.8, March 1992.

[10] Borgnakke, C. and Larsen, P. S.; Statistical Collision Model for Monte Carlo Simulation of Polyatomic Gas Mixture. *Journal of Computational Physics*, Vol. 18, No. 4, 1975, pp. 405-420.

[11] *Hypersonic Experimental and Computational Capability, Improvement and Validation.* AGARD AR 319, edited by J. Muylaert, A. Kumar, and C Dujarric, Vol. II, Dec. 1998.

[12] Candler, G. V., Nompelis, I., and Holden, M. S.; Computational Analysis of Hypersonic Laminar Viscous-Inviscid Interactions. AIAA Paper 2000-0532, Jan. 2000.

[13] Holden, M.; Experimental Studies of Laminar Separated Flows Induced by Shock Wave/Boundary Layer and Shock/Shock Interaction in Hypersonic Flows for CFD Validation. AIAA Paper 2000-0930, Jan. 2000.

[14] Chanetz, B.; *Study of Axisymmetric Shock Wave/Boundary Layer Interaction in Hypersonic Laminar Flow.* ONERA Technical Report TR No. 42/4623, Feb. 1995.

[15] Needham, D., and Stollery, J.; Boundary Layer Separation in Hypersonic Flow. AIAA Paper 66-455, 1966.

[16] Markelov, G. N., Kudryavtsev, A. N., and Ivanov, M. S.; Continuum and Kinetic Simulation of Laminar Separated Flow at Hypersonic Speeds. *Journal of Spacecraft and Rockets*, Vol. 37, No. 4, July-August 2000, pp. 499-506.

[17] Ames Research Staff; *Equations, Tables, and Charts for Compressible Flow.* NACA Report 1135, 1953.